







RESEARCH ARTICLE | FEBRUARY 02 2023

# Deciphering strontium sulfate precipitation via Ostwald's rule of stages: From prenucleation clusters to solution-mediated phase transformation

Special Collection: [Nucleation: Current Understanding Approaching 150 Years After Gibbs](#)

A. R. Lauer; R. Hellmann ; G. Montes-Hernandez ; N. Findling; W. L. Ling ; T. Epicier; A. Fernandez-Martinez ; A. E. S. Van Driessche  

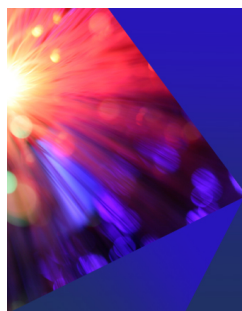


*J. Chem. Phys.* 158, 054501 (2023)

<https://doi.org/10.1063/5.0136870>



CrossMark



The Journal of Chemical Physics  
2024 Emerging Investigators  
Special Collection

Submit Today

# Deciphering strontium sulfate precipitation via Ostwald's rule of stages: From prenucleation clusters to solution-mediated phase transformation

Cite as: J. Chem. Phys. 158, 054501 (2023); doi: 10.1063/5.0136870

Submitted: 29 November 2022 • Accepted: 10 January 2023 •

Published Online: 2 February 2023



View Online



Export Citation



CrossMark

A. R. Lauer,<sup>1</sup> R. Hellmann,<sup>1</sup>  G. Montes-Hernandez,<sup>1</sup>  N. Findling,<sup>1</sup> W. L. Ling,<sup>2</sup>  T. Epicier,<sup>3</sup>  
A. Fernandez-Martinez,<sup>1</sup>  and A. E. S. Van Driessche<sup>1,4,a)</sup> 

## AFFILIATIONS

<sup>1</sup> Université Grenoble Alpes, Université Savoie Mont Blanc, CNRS, IRD, ISTERRE, 38000 Grenoble, France

<sup>2</sup> Université Grenoble Alpes, CEA, CNRS, IBS, F-38000 Grenoble, France

<sup>3</sup> Université de Lyon, Université Claude Bernard Lyon1, IRCELYON, umr CNRS 5256, 69626 Villeurbanne Cedex, France

<sup>4</sup> Instituto Andaluz de Ciencias de la Tierra (IACT), CSIC – University of Granada, Armilla, Granada E-18100, Spain

**Note:** This paper is part of the JCP Special Topic on Nucleation: Current Understanding Approaching 150 Years After Gibbs.

**a)** Author to whom correspondence should be addressed: [alexander.vd@csic.es](mailto:alexander.vd@csic.es)

## ABSTRACT

Multiple-step nucleation pathways have been observed during mineral formation in both inorganic and biomineral systems. These pathways can involve precursor aqueous species, amorphous intermediates, or metastable phases. Despite the widespread occurrence of these processes, elucidating the precise nucleation steps and the transformation mechanisms between each step remains a challenging task. Using a suite of potentiometric, microscopic, and spectroscopic tools, we studied the nucleation pathway of  $\text{SrSO}_4$  as a function of the physico-chemical solution parameters. Our observations reveal that below a threshold supersaturation, nucleation is driven by bound species, akin to the prenucleation cluster model, which directly leads to the formation of the stable phase celestine,  $\text{SrSO}_4$ . At higher supersaturations, this situation is altered, with nucleation dominated by the consumption of free ions. Importantly, this change in nucleation mechanism is coupled to the formation of a hemihydrate metastable phase,  $\text{SrSO}_4 \cdot 1/2\text{H}_2\text{O}$ , which eventually transforms into celestine, adhering to Ostwald's rule of stages. This transformation is a solution-mediated process, also occurring in the presence of a fluid film and is controlled by the physico-chemical parameters of the surrounding environment. It proceeds through the dissolution of the metastable phase and the *de novo* crystallization of the final phase. Overall, our results reveal that ion association taking place during the prenucleation stage dictates whether the nucleation pathway goes through an intermediate phase or not. This also underlines that although Ostwald's rule of stages is a common process, it is not a prerequisite for mineral formation—even in systems where it can occur.

© 2023 Author(s). All article content, except where otherwise noted, is licensed under a Creative Commons Attribution (CC BY) license (<http://creativecommons.org/licenses/by/4.0/>). <https://doi.org/10.1063/5.0136870>

## I. INTRODUCTION

Recent experimental studies have highlighted the importance of complex, and in particular multiple-step, nucleation pathways to mineral formation in both natural and engineered environments.<sup>1</sup> Such nucleation schemes have been suggested as a means for the concentration, transportation, and/or temporary storage of ions during biomineralization.<sup>2,3</sup> They have also been used to describe

the behavior of inorganic solutions with high supersaturation, e.g., Ref. 4. A variety of distinct nucleation pathways that entail the formation of intermediate phases have been described thus far, ranging from nano-crystal aggregation e.g., Ref. 5, to amorphous particle integration, e.g., Ref. 6, to ion-complex agglomeration, e.g., Ref. 7. Many of these precursor phases, or intermediates, are aqueous species that are not taken into account by current thermodynamic speciation models, simply due to the lack of thermochemical data

about them, which can be difficult to obtain due to the short-lived character of the species (e.g., transient polynuclear clusters<sup>8–10</sup>). In other cases, an amorphous precipitate is formed, which is typically considered to be a thermodynamic phase via the determination of an effective solubility constant.<sup>11</sup> However, some studies have shown that the stoichiometry of these amorphous precipitates can vary during the precipitation process, making them questionable thermodynamic phases.<sup>11,12</sup> Often, the precipitation pathway goes through the formation of one (or multiple) discrete metastable phase(s), a concept introduced by Ostwald in 1897,<sup>13</sup> and commonly referred to as “Ostwald’s rule of stages.” Intermediate phases, either amorphous or crystalline, can be sufficiently long-lived, thus allowing their physico-chemical characterization. Nonetheless, even in such cases, elucidating the transformation reaction to the more stable phase, e.g., through a solid-state reaction or fluid-mediated reaction, remains a challenging task, e.g., Ref. 1.

Despite the widespread interest and relevance of (re-) examining nucleation pathways in natural and engineered environments, the formation mechanisms of sulfate minerals (which comprise ~7% of known minerals in the earth crust<sup>14</sup>) have received surprisingly little attention—with the only exception being calcium sulfate.<sup>8,15,16</sup> Strontium sulfate is abundant in various earth surface environments, with concentrations reaching saturation in marine sediment porewaters in varied geological settings.<sup>17</sup> Additionally, the precipitation of SrSO<sub>4</sub> solid phases is an important factor in the design of offshore oil wells in order to avoid scaling and clogging.<sup>18,19</sup> The anhydrous mineral form, celestine (SrSO<sub>4</sub>), is the principal ore of strontium and is the starting material for the production of strontium metal and nearly all strontium salts. Sulfates are also used in pyrotechnics and ceramics.<sup>20</sup> Moreover, strontium sulfate can also form as a biomineral, constituting the shells of several acantharian protozoa.<sup>21</sup> At the present, relatively little is known about the formation mechanisms of celestine. Some studies reported its precipitation within the scope of classical nucleation theory, e.g., Refs. 22–24, while others have merely focused on quantifying the nucleation kinetics of celestine.<sup>25–31</sup> The effect of additives<sup>32–35</sup> on the nucleation and growth of celestine has also been examined. It is interesting to note that a transient strontium sulfate phase was described as early as 1926.<sup>36</sup> Until now, this intermediate has only been isolated and characterized as a partially hydrated phase, SrSO<sub>4</sub> · 1/2H<sub>2</sub>O<sup>37</sup> (for simplicity, it will be referred to as “hemihydrate” for the remainder of this document). It has been shown that the formation of this phase is controlled by the degree of fluid supersaturation as well as the presence of silicon in solution.<sup>38</sup> Despite these studies centered on the metastable phase, virtually no attention has been directed to the role the hemihydrate plays in the formation of celestine.

In this work, we deciphered the different steps of the precipitation process of strontium sulfate from aqueous solutions, including the precursor and intermediate phases, and established the nucleation pathways as functions of the physico-chemical parameters. In addition, we performed a detailed characterization of strontium sulfate hemihydrate, unveil conditions that lead to an elevated kinetic persistence of the phase, and demonstrated that dissolution-reprecipitation is the most likely mechanism controlling the transformation of the hydrated metastable phase to anhydrous celestine, the final stable phase. Here, we make progress toward a cohesive understanding of nucleation processes obeying Ostwald’s rule of stages, and in particular, the (trans)formation of hydrated to

anhydrous sulfate minerals in particular, through a careful investigation of fluid-mediated reactions taking place in the SrSO<sub>4</sub>–H<sub>2</sub>O system.

## II. MATERIALS AND METHODS

### A. Precipitation of intermediate and final SrSO<sub>4</sub> phases

All solutions used for the precipitation experiments were created by mixing equal volumes of equimolar solutions (100 mM) of SrCl<sub>2</sub> (99% extra-pure SrCl<sub>2</sub> · 6H<sub>2</sub>O, Acros Organics) and Na<sub>2</sub>SO<sub>4</sub> (≥99% purity, Roth) dissolved in deionized water. The saturation index with respect to pure celestine –  $\Omega = \log[a(\text{Sr}^{2+}) \cdot a(\text{SO}_4^{2-})/K_{\text{sp,celestine}}]$ , where  $a(\text{Sr}^{2+})$  and  $a(\text{SO}_4^{2-})$  are the activities of the Sr<sup>2+</sup> and SO<sub>4</sub><sup>2-</sup> ions in solution, and  $K_{\text{sp,celestine}}$  is the solubility product of celestine (10<sup>–6.62</sup>)—was calculated for all solutions using the code Phreeqc and the BRGM Thermoddem geochemical database.

The optical characterization of the nucleation reaction was conducted with a UV-VIS Cary 3500 (Agilent) instrument. Strontium sulfate precipitation experiments were carried out by mixing equal volumes of SrCl<sub>2</sub> and Na<sub>2</sub>SO<sub>4</sub> stock solutions into a 100 mM NaCl solution (to maintain a constant background ionic strength). In all cases, the final solution had a volume of 2 ml, and the SrSO<sub>4</sub> concentration varied from 3.5 to 15 mM. The solutions were mixed directly in a standard 12.5 × 12.5 mm<sup>2</sup> poly(methylmethacrylate) (PMMA) cuvette (BRAND GmbH) and agitated with a magnetic stirrer at 800 rpm. Time-resolved absorbance curves were collected at a wavelength length of 500 nm.

The evolution of the ionic environment during the early stage of strontium sulfate nucleation was probed via potentiometric titration experiments. For these experiments, equimolar concentrations of the previously described SrCl<sub>2</sub> and Na<sub>2</sub>SO<sub>4</sub> solutions were dosed at controlled rates into 50 ml of deionized water in a reactor vessel that was continuously mixed with a magnetic stirrer bar at 500 rpm. Dosing rates were controlled by a Metrohm 905 Titrando equipped with two 800 Dosino devices, each utilizing a 20 ml dosing unit. The evolution of the precipitation reaction was continuously monitored based on solution turbidity (Metrohm optrode), conductivity (Metrohm 5-ring conductivity measuring cell), and cation concentration (Ion Selective Electrode that consisted of two half-cells: a Mettler-Toledo DX337 membrane and a Metrohm LL ISE reference electrode).

The solid phases (hemihydrate and celestine) obtained after mixing the equimolar solutions were isolated at different time points of the precipitation reaction by a fast vacuum filtering process employing filtration membranes (0.5 μm). To obtain nearly pure hemihydrate, equal volumes of equimolar solutions of 100 mM SrCl<sub>2</sub> and 100 mM Na<sub>2</sub>SO<sub>4</sub> (i.e., 50 mM SrSO<sub>4</sub> with 100 mM NaCl,  $S = 2.6$ ) were added directly to the filtering apparatus and gently stirred by hand for ~5 s until the hemihydrate resembled a gel and appeared relatively stable. At this point, water was then rapidly removed via a vacuum system. Once there was no visible presence of water, EtOH (95% v/v, Fisher) was added to remove background salts and halt any further reactions. A total of three EtOH rinses were completed for each sample. After the third rinse and a vacuum assisted drying process, the remaining solid phase cake was ground

for further analyses. Importantly, the filtration and cleaning steps did not significantly alter the phase(s) being isolated (see results for details).

## B. Characterization of solid samples

### 1. Powder x-ray analysis

The composition of the solid samples was first evaluated with powder x-ray diffraction (PXRD). PXRD patterns were recorded with a Bruker D8 powder diffractometer equipped with a SolXE Si(Li) solid state detector from Baltic Scientific Instruments using  $\text{CuK}\alpha_{1,2}$  radiation. Intensities were recorded at  $0.026^\circ$  two-theta step intervals from  $5^\circ$  to  $90^\circ$  with 6 s counting time per step. Data were evaluated using the code DIFFRAC.EVA (Bruker) for comparison to previously published structures (ICDD PDF 00-005-0593 for celestine and ICSD 167 054 for hemihydrate). Approximately 1 g of powder was analyzed for each sample. The analyzed celestine powder had a granulometry  $<50 \mu\text{m}$ . The hemihydrate was broken up as much as possible inside a plastic beaker using a spatula to produce a fine-grain powder (hemihydrate rapidly transformed to celestine when using a sieve or mortar and pestle). For other *ex situ* characterizations of the hemihydrate, such as those by infrared spectroscopy, were confirmed by PXRD to be  $>95\%$ . For the celestine samples, only those where no hemihydrate was identified (purity  $>99\%$ ) were used for further characterization.

### 2. Fourier-transform infrared spectroscopy (FTIR)

Fourier-transform infrared spectroscopy was performed to obtain spectral information that was used to confirm the presence of hemihydrate in mixed systems. FTIR analysis was performed in ATR mode (Thermo Scientific Nicolet iS50). Dry and wet powder samples were placed on the diamond window. Dry powders were gently compressed to achieve maximum surface contact with the diamond window, while suspended powders were allowed to remain dispersed. The spectra were normalized to the highest absorbing peak (neglecting noise due to high degrees of water absorbance in wet samples at wavenumbers  $400\text{--}800 \text{ cm}^{-1}$ ). The spectra were evaluated for peak shifts, shape changes, and peak ratio inversions that allowed for the differentiation of hemihydrate from celestine.

### 3. Electron microscopy

A variety of electron microscopy techniques were used to characterize the hemihydrate and celestine. Hemihydrate and celestine powders were dispersed directly onto metal stubs with an affixed conductive carbon tape; no coatings were applied. Samples were observed with scanning electron microscopy (SEM) and field emission gun SEM (FEG-SEM). Low-resolution SEM was carried out using a Vega 3 Tescan instrument at 16.0 kV, while FEG-SEM was conducted on a Zeiss Ultra 55 FEG-SEM at 3 kV.

Cryogenic Transmission Electron Microscopy (cryo-TEM) images were acquired with a Ceta CMOS camera under low-dose conditions on a Thermo Fischer Tecnai F20 TEM operating at 200 keV. Samples were prepared by placing  $4 \mu\text{l}$  aliquots of the reaction solution on glow discharged Quantifoil or lacey carbon film grids, and then vitrified using a Thermo Fisher Vitrobot Mark IV system. Blotting times were adjusted to obtain appropriate ice thicknesses.

High-resolution transmission electron microscopy (HRTEM) observations were made with a Cs-corrected FEI Titan ETEM G2

80–300 kV (for this work, images were acquired under vacuum conditions typical of non-environmental TEM). Samples were prepared by dispersing a small amount of hemihydrate in alcohol, placing a droplet of suspension on a TEM grid, and evaporating the excess EtOH in a bell jar pumped down using a low vacuum primary pump. Imaging was carried out at 80 and 300 kV. According to specific irradiation tests, it was concluded that the hemihydrate material could bear electron doses up to  $10^4 \text{ e}^- \text{ \AA}^{-2}$  with a typical low electron flux of about  $50 \text{ e}^- \text{ \AA}^{-2} \text{ s}^{-1}$  at 300 kV without significant observable damage. This corresponds to a maximum of about 3 min of continuous illumination without any detectable morphological changes.  $4 \times 4 \text{ k}^2$  images were recorded with an advanced CMOS Oneview camera (Gatan) after a few seconds of exposure to the electron beam, with cumulative acquisitions of about 1 s based on an average of 40–120 ms elementary frames. Thus, images were collected over much shorter time periods than the aforementioned limits associated with observable damage occurring.

We performed crystallographic identification of selected TEM micrographs using FFT of high-resolution micrographs instead of selected area electron diffraction (SAED) patterns. One of the advantages of using a Cs-corrected TEM is its superior spatial resolution, which facilitates lattice plane imaging, even along more or less exotic azimuths. Numeric Fourier transforms can then be used to provide diffraction spots, allowing classical indexing. This methodology allowed us to directly select single fibers or particles for analysis, including even very local, nanometer-sized areas within such objects—doing the same with SAED would require a highly focalized beam that could result in beam damage. With this technique, we were, therefore, able to remain in imaging mode (rather than switching between imaging and diffraction modes) and avoid significant irradiation effects under the illumination conditions used here.

## C. In situ analyses of solid phase transformation

### 1. FTIR and Raman

*In situ* observations were conducted both with FTIR and Raman spectroscopy. For the FTIR-based experiments, 2 ml of the previously described 50 mM  $\text{SrSO}_4$  solution was prepared. After the precursor gel formed, excess water was removed with a pipette to halt the reaction, and a small quantity of gel was transferred, using a spatula (without compression), onto a diamond crystal for ATR mode analysis. To restart the reaction again, a droplet of deionized water was added to replicate the solution conditions of the reaction beaker where the gel phase initially formed. Each final spectrum represents the average of 15 individual scans conducted in 20-s intervals using a Nicolet iS50 FTIR Spectrometer (Thermo Scientific) configured with a DLaTGS detector (KBr window).

Raman spectroscopy was conducted on a solution made by combining 100 ml of each of the two 100 mM stock solutions ( $\text{Na}_2\text{SO}_4$  and  $\text{SrCl}_2$ ) and mixing the resulting (200 ml) solution. The *in situ* Raman measurements of the solution were carried out in a custom-built 600 ml Hastelloy C22 Parr reactor with an integrated Raman probe (Optical Systems Raman RXN1; for a detailed description of this setup, see Montes-Hernandez and Renard<sup>39</sup>). Spectra were collected from 100 to  $3425 \text{ cm}^{-1}$ , averaging three scans over 15 s with a time interval of 1 min between scans. Under these conditions, only one sulfate peak was readily observable, so evaluation was focused on the wavenumber band from 965 to  $1025 \text{ cm}^{-1}$ . To

initiate the precipitation reaction, the suspensions were mixed for  $\sim 1$  s at 300 rpm using a twin-bladed mixer, followed by mixing at 50 rpm—this served to slow down the transformation reaction while providing sufficient agitation to homogenize the solution and minimize the risk of measuring local anomalies. The shown spectra represent the average of three measurements over  $\sim 5$  s, and unless specified otherwise, only untreated data have been presented here.

## 2. Electrochemical probes

An additional *in situ* direct mixing experiment was conducted using electrochemical probes. 150 ml of the 50 mM  $\text{SrSO}_4$  solution was prepared in a 250 ml beaker (75 ml of 100 mM  $\text{Na}_2\text{SO}_4$  added to 75 ml of 100 mM  $\text{SrCl}_2$ ) and mixed with a 2 cm PTFE-coated stirrer bar (50 rpm). The reaction was monitored with a Metrohm 5-ring conductivity measuring cell ( $c = 0.7 \text{ cm}^{-1}$  with Pt1000; part no. 6.0915.100), a Metrohm optrode (part no. 6.115.000), and an ion selective electrode (ISE) that consisted of two half-cells: a polymer membrane cation ISE with a silver/silver chloride reference electrode. Probes were connected to a Metrohm 905 titration unit and controlled by Tiamo 2.5 software.

## 3. Powder x-ray diffraction (PXRD)

*In situ* PXRD was conducted in a TTK Anton Paar chamber with a ProUmid humidity controller. Samples were kept at  $23^\circ\text{C}$  during data collection, whereas the desired relative humidity value (RH) was maintained ( $\pm 2\%$  RH) by using a constant flow of mixed dry/saturated air. RH was continuously monitored with a hygrometer located next to the sample. Samples were equilibrated at the desired humidity (ranging from 70% to 90%) for a minimum of 10 min before starting data collection.

To increase the time resolution, counting times were reduced to 3 s, and scanning was limited to the  $2\theta$  ranges from  $12^\circ$  to  $16^\circ$  and  $30^\circ$ – $34^\circ$  in order to focus on one unique peak for hemihydrate ( $14.28^\circ$ ) and one unique peak for celestine ( $32.79^\circ$ ). The mass fractions of the phases were estimated using a semi-quantitative reference intensity ratio (RIR) technique,<sup>40,41</sup> based on XRD peak intensities (peak heights) and defined by

$$I_a = \frac{K_a x_a}{\mu_s \rho_a},$$

where  $K_a$  is a material parameter for phase  $a$ ,  $\rho_a$  is the density of the phase,  $\mu_s$  is the permittivity of the entire sample, and  $x_a$  is the mass fraction of phase  $a$ . Taking the ratio of the intensity of each respective peak of interest for the two different phases and grouping the material constants (including density) into a single term,  $K$ , the mass fraction of a phase can be determined solely from the ratio of the two peak heights,

$$\frac{I_a}{I_b} = \frac{K_a x_a \rho_b}{K_b x_b \rho_a} = K \frac{x_a}{x_b}.$$

In the absence of additional phases,  $x_a + x_b = 1$ , and assuming that  $\frac{I_a}{I_b} = R$ , then

$$x_a = \frac{R}{K + R} \quad \text{and} \quad x_b = \frac{K}{K + R}.$$

The intensities of the peaks  $I_a$  and  $I_b$  that were tracked in this experiment are located at  $2\theta = 14.26$  for hemihydrate and  $32.78$  for

celestine. At the end of the experiment, a full spectrum was taken, and Rietveld integration was used to estimate the final concentrations  $x_a$  and  $x_b$ . These concentrations and the intensities  $I_a$  and  $I_b$  from the last *in situ* time point were used to determine  $K$  for each experiment.

For the experiments at 70% and 80% relative humidity, it was found that  $I_a/I_b$  in the full spectrum at the end of the experiment matched the  $I_a/I_b$  ratio after  $\sim 9$  h. The calculations were repeated using that time point as a reference, and the difference between the two estimations of concentration was subsequently used as an estimate of the error. For the experiment at 90% humidity, no such “ratio matching” point existed, so the error was assumed to be the maximum found at any point during the two lower humidity experiments.

## 4. Optical microscopy

An optical microscopic visualization of the transformation from the hemihydrate to celestine was conducted using a Leica M125 microscope equipped with a ring light and backlight illumination. The reaction was conducted in a silica glass capillary (Vitrex Medical) with the following dimensions: inner diameter = 1.42 mm, outer diameter = 1.80 mm, and length = 75 mm. One end of the capillary was briefly dipped into molten paraffin wax to form a seal, followed by the introduction of 100 mM  $\text{Na}_2\text{SO}_4$  into half of the capillary, then 100 mM  $\text{SrCl}_2$  to fill the remaining half of the capillary, leaving a diffusion front in the center, and finally, the other end of the capillary was sealed. A simple schematic of this experimental setup can be found alongside the results of the experiment (Fig. 7). The formation of the hemihydrate occurred within the first seconds after the introduction of the  $\text{SrCl}_2$ , such that crystals could be seen by the naked eye at the time that the capillary was sealed (5–10 s after injection). The sealed capillary was subsequently placed under the microscope with an alignment and focusing procedure that took  $\sim 2$  min. Images monitoring the transformation from hemihydrate to celestine were acquired approximately every 20 s for a duration of 6 h.

## III. RESULTS AND DISCUSSION

### A. Nucleation pathways in the $\text{SrSO}_4$ - $\text{H}_2\text{O}$ system

We studied the nucleation pathway of  $\text{SrSO}_4$  at different degrees of supersaturation. This was accomplished through direct mixing experiments [Fig. 1(a)] and potentiometric co-titrations (Fig. 2). Powder x-ray diffraction of the precipitates [Fig. 1(b)] indicated that the first solid phase to appear depends on the initial supersaturation of the reaction. At the lowest supersaturations tested, a direct nucleation pathway was followed, resulting in the precipitation of celestine without observable intermediates. At the highest supersaturations, a two-step pathway occurred where a metastable hemihydrate formed first, followed by the thermodynamically more favorable anhydrous phase (a detailed characterization of both solid phases is provided in Sec. III B). The lower limit for the formation of the hemihydrate was determined to be  $\sim 9$ – $10$  mM (corresponding to a saturation index of  $\Omega = 1.55$  with respect to celestine). This limit was determined through direct mixing experiments that took place in a UV-Vis cuvette with agitation at 800 rpm. As seen in Fig. 1(a), the shape of the absorbance vs time curves changes at the 9–10 mM limit. At higher concentrations, there is a peak and an inflection point in the absorbance curve after initial nucleation. This coincides

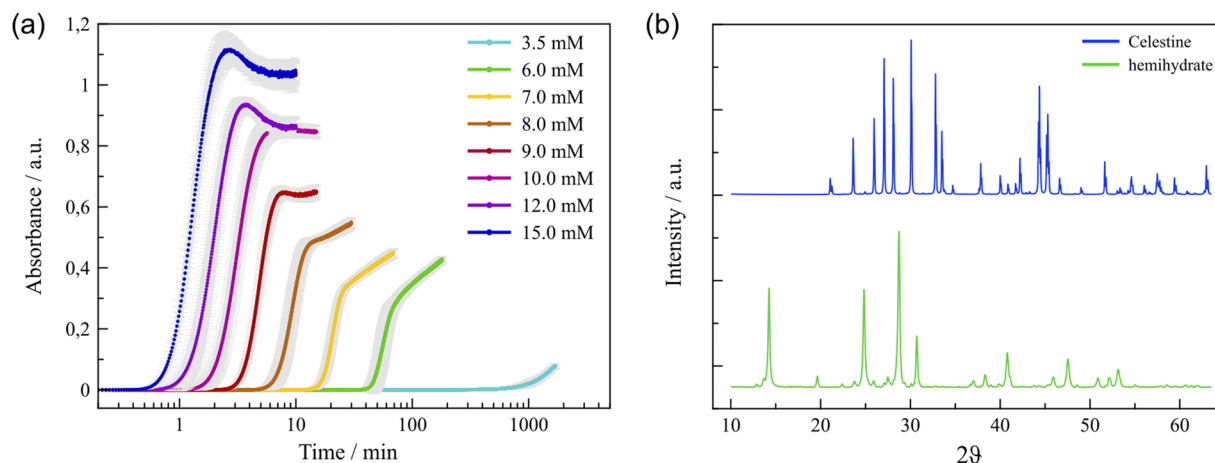


**FIG. 1.** Precipitation of solid phases in the  $\text{SrSO}_4\text{-H}_2\text{O}$  system. (a) UV-Vis absorbance curves measure induction times as a function of the initial  $\text{SrSO}_4$  concentration. (b) PXRD spectra of the celestine ( $\text{SrSO}_4$ ) and hemihydrate ( $\text{SrSO}_4 \cdot 1/2\text{H}_2\text{O}$ ).

with a maximum concentration of the high-surface area needles that characterize hemihydrate, which then subsequently dissolved and formed celestine (this transformation process is discussed in detail in Sec. III C). Below the 9–10 mM limit, all of the absorbance curves reveal just an increase in turbidity, which can be attributed to the direct nucleation and growth of celestine. This limit was corroborated by monitoring the sulfate concentration using *in situ* Raman (see Sec. III C). From these induction time measurements, an effective interfacial energy for celestine of  $35 \text{ mJ m}^{-2}$  was obtained (Fig. S1), which compares well with previously reported values (Table S1). We also estimated the interfacial energy for hemihydrate (Fig. S1),  $\sim 3 \text{ mJ m}^{-2}$ , which is considerably lower than that of celestine.

In order to probe the evolution of the ionic environment during the early stage of strontium sulfate nucleation, equimolar concentrations of  $\text{SrCl}_2$  and  $\text{Na}_2\text{SO}_4$  were co-titrated at a steady rate into a reaction vessel containing 50 ml of deionized water, and the resulting electrolyte solution was continuously monitored for cation concentration, turbidity, and conductivity. The first stage of these co-titrations is characterized by a monotonic increase of  $\text{Sr}^{2+}$  activity and solution conductivity and a maximum steady-state transmittance signal [Fig. 2(a)]. During this first stage, the detected amount of free  $\text{Sr}^{2+}$  is lower than the total added strontium, indicating the presence of bound ions.<sup>42</sup> Note also that these two curves increasingly diverge with time. A second stage is reached when the transmittance abruptly decreases, followed by a change in the shape of the free ions [Fig. 2(a)] and conductivity curves (data not shown). These changes correspond to the onset of nucleation and the critical supersaturation ( $\Omega_{\text{crit}}$ ) at which this occurred. The critical supersaturation was controlled by varying the ion addition rate [i.e., at higher addition rates, higher critical supersaturations are reached, and vice versa, Fig. 2(b)].

The data shown in Fig. 2 reveal some important mechanistic information. There is a significant difference between the nucleation times measured by the transmittance probe and those measured by the ISE and conductivity probes [inset Fig. 2(a)]. At the lowest  $\Omega_{\text{crit}}$  the transmittance probe detected the formation of a new

phase significantly before the ISE and conductivity probe registered the consumption of free ions [Fig. 2(b)]. This observation indicates that the onset of strontium sulfate nucleation occurs via the consumption of bound, i.e., neutral species ( $\text{SrSO}_4^0$  or larger) that go undetected by the ISE and conductivity probe. Consequently, the particles detected by the transmittance probe are formed through the aggregation of neutral particles, the smallest of which could be ion pairs. At the two highest  $\Omega_{\text{crit}}$ , the early detection of nucleation by the transmittance probe vanishes [Fig. 2(c)], and the first stage of nucleation is mainly driven by ion consumption and not by neutral bound species. In a previous study,<sup>42</sup> we provided a tentative explanation for the change in dominant species controlling the early stages of nucleation: according to MeNT modeling, the presence of some pre-nucleation species can be described by a kinetic “slow step” that results in relatively long-lived species that do not require a thermodynamic minimum. Thus, as the reaction accelerates, the importance of the kinetically apparent species diminishes.

Thus, these co-titration experiments, conducted at different addition rates, reveal that below a threshold supersaturation, the onset of nucleation is dominated by the consumption of bound species (ion pairs or larger), akin to the prenucleation clusters (PNCs) observed for  $\text{CaSO}_4$ ,<sup>8,9</sup>  $\text{CaCO}_3$ ,<sup>43</sup>  $\text{CaPO}_4$ ,<sup>44</sup> or  $\text{Mg}(\text{OH})_2$ ,<sup>45</sup> among others. Above this threshold supersaturation, the onset of nucleation is characterized by the consumption of both bound and unbound species. Of significant note here, the threshold supersaturation at which this change in nucleation pathway occurs corresponds to a critical supersaturation ( $\Omega \approx 1.55$ ) when the intermediate phase (hemihydrate) starts to form. This suggests that the reaction step related to the consumption of bound species diminishes in importance as the rate of the reaction increases, similar to the MeNT prediction for the behavior of prenucleation species. Overall, these results suggest that changes in the system during the prenucleation phase are coupled to a pathway that forms via a metastable intermediate phase or not. It could be argued that it is energetically more favorable to form a hydrated phase from fully solvated charged ions than from ion pairs/PNCs that have already removed part

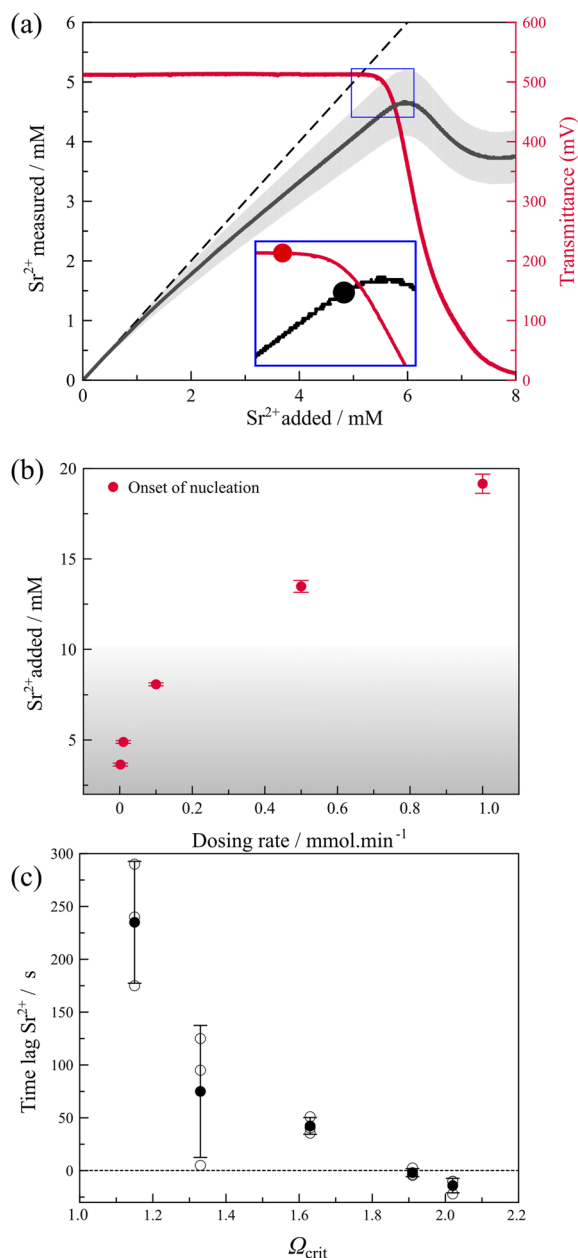


**FIG. 2.** Evolution of the ionic environment during the early stage of strontium sulfate nucleation. (a) Cation  $\text{Sr}^{2+}$  concentration as measured by an ion selective electrode (black, gray shaded area represents the standard deviation of three replicate experiments), and optical transmittance of the solution (red) measured *in situ* during an equimolar co-titration experiment. For reference, the total added strontium concentration is also shown (dashed line). (b) Concentration at the onset of nucleation determined by the transmittance probe for each dosing rate of  $\text{SrSO}_4$  in the co-titrations tested in this study. The gray area denotes the concentration range where celestine is formed directly. Error bars represent the standard deviation of three replicate experiments. (c) Difference in measured nucleation induction time determined by transmittance and ISE probes as a function of  $\Omega_{\text{crit}}$ . A positive difference means the transmittance probe detected the phase transition first (i.e., before the ISE probe). The gray dotted line corresponds to equal induction times. Error bars represent the standard deviation of three replicate experiments.

of their hydration shell (compared to ions), which would explain why celestine nucleation is driven by bound species and hemihydrate formation is dominated by charged ions.<sup>46</sup> In summary, the experimental observations discussed above reveal that as the supersaturation rate, and thus also the critical supersaturation, increases during  $\text{SrSO}_4$  co-titrations, the preferred nucleation mechanism changes.

## B. Characterization of the solid phases forming in the $\text{SrSO}_4\text{-H}_2\text{O}$ system

As discussed above, during the precipitation of  $\text{SrSO}_4$  from highly supersaturated solutions ( $\Omega > 1.55$ ) an intermediate phase is formed first, which subsequently transforms into the stable anhydrous phase. In order to characterize the two solid phases and track their temporal evolution, we selected a specific reaction condition (50 mM  $\text{SrSO}_4$ ,  $\Omega = 2.60$ ) where the solution turbidity rapidly increases within 1–2 s upon mixing of both reactants ( $\text{SrCl}_2$  and  $\text{Na}_2\text{SO}_4$ ), due to the formation of precipitates that aggregate into white, cloud-like emulsions. These aggregates increase in concentration until a gel-like concentrate is formed. This gel concentrate is composed of the intermediate hemihydrate, and over time ( $\sim 100$  min), it is fully replaced with particles that settle to the bottom of the reactor vessel. Below, we describe the different strontium sulfate phases, followed by details on the transformation of the intermediate hydrous phase to the final celestine phase (Sec. II C).

Using our isolation protocol (see “Materials and methods”), we were able to obtain (>99%) pure samples of both phases. Powder x-ray diffraction and Rietveld refinement were used to identify and quantify both phases [Fig. 1(b)]. The hemihydrate phase crystallizes in the hexagonal system, with unit cell dimensions of  $a = 7.178$  and  $c = 6.589$  Å, confirming previously reported data.<sup>38</sup> The  $c$  axis lies parallel to the axial direction of the needle-like fibers. In contrast, anhydrous celestine crystallizes in the orthorhombic system and has the following cell parameters:  $a = 8.360$  Å,  $b = 5.352$  Å,  $c = 6.858$  Å (PNMA).<sup>47</sup> Detailed structural analyses (see Table S2) revealed that the crystalline intermediate phase, hydrated strontium sulfate, contains half a molecule of water per molecule of strontium sulfate ( $\text{SrSO}_4 \cdot 1/2\text{H}_2\text{O}$ ). This is analogous to the hemihydrate of calcium sulfate (bassanite;  $\text{CaSO}_4 \cdot 1/2\text{H}_2\text{O}$ ), which is a common intermediate phase during gypsum ( $\text{CaSO}_4 \cdot 2\text{H}_2\text{O}$ ) or anhydrite ( $\text{CaSO}_4$ ) formation.<sup>5,48,49</sup>

SEM imaging [Figs. 3(a) and 3(b)] of the hemihydrate and celestine phases reveals a distinct morphological difference between the two, the former being fibrous with a very high aspect ratio ( $L/W > 100$ ) and the latter being prismatic. The high density of these fibrous aggregates is most likely responsible for the gel-like phase observed in solution. Importantly, cryo-TEM [Fig. 3(c)] imaging of aliquots retrieved from the early stages of the reaction further reveals the extreme elongated morphology of the hydrate phase, which, quite surprisingly, shows evidence for non-brittle behavior by bending of the thinnest crystals [see inset Fig. 3(c)]. This property may contribute to the entanglement of these fibers and the formation of the observed gel-like nature of the initial precipitate. Cryo-TEM images of aliquots collected at the end of the reaction showed prismatic celestine crystals [Fig. 3(d)]. HRTEM imaging and fast Fourier transforms [Figs. 3(e) and 3(f)] confirm the respective microstructural equivalence of the hemihydrate and celestine

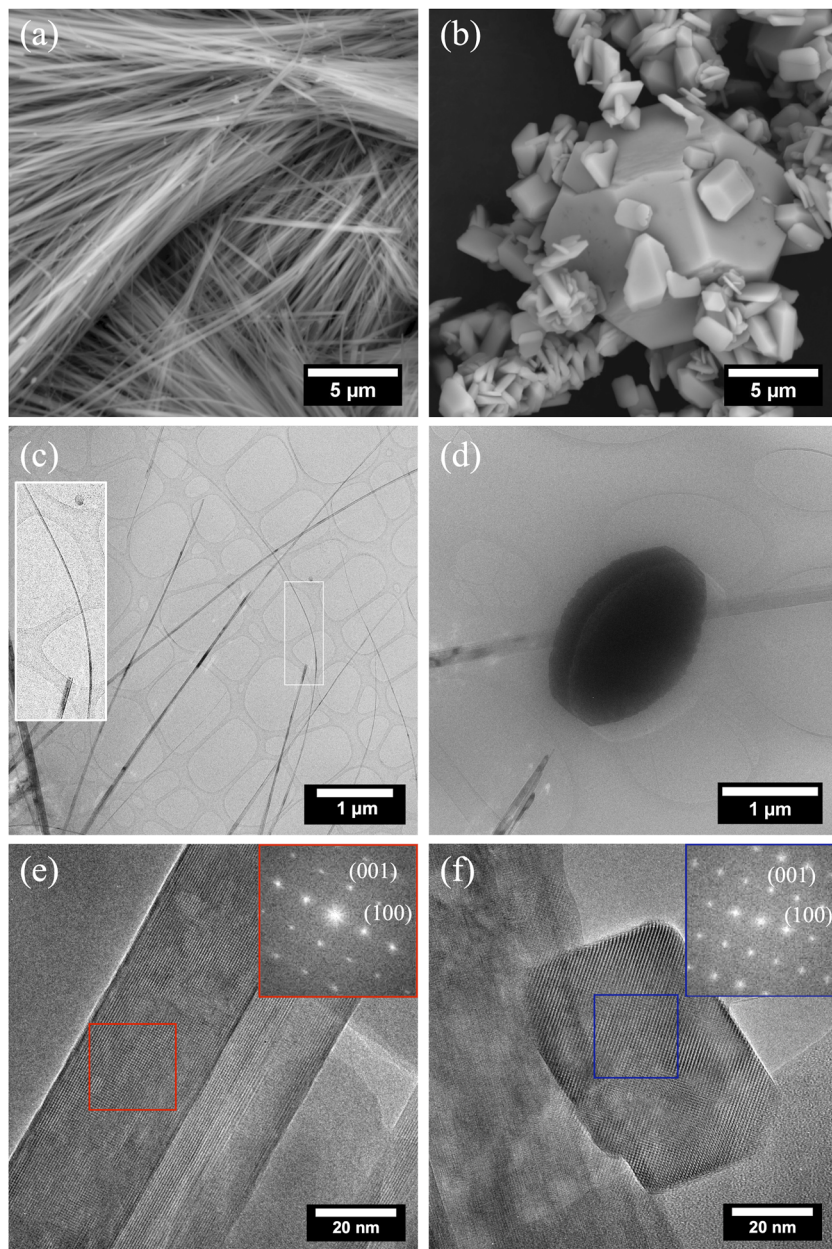


**FIG. 3.** Characterization of the solid phases forming during  $\text{SrSO}_4$  precipitation from solutions using electron microscopy. SEM image of bundled fibrous hemihydrate phase (a) and celestine crystals (b) in a variety of morphologies and sizes. Cryo-TEM images of hemihydrate fibers (c) and a celestine crystal (d). HRTEM images of a hemihydrate fiber (e) and a celestine crystal adjacent to a hemihydrate fiber (f). The corresponding FFT of selected areas (red, blue boxes) of the respective crystals is shown in insets, and the spots on the FFT patterns indicate the crystallographic planes.

observed in both TEM experiments with that measured by x-ray diffraction. Importantly, the cryo-TEM and *ex situ* SEM and TEM images all reveal the same morphologies for the hemihydrate and the celestine, demonstrating that the filtration and cleaning steps do not significantly alter the phase being probed. Furthermore, no obvious structural/epitaxial relationship was observed between the two phases.

*Ex situ* FTIR [Fig. 4(a)] analyses of both phases shows two characteristic  $\text{SO}_4$  vibrations, at  $\sim 600$  and  $\sim 1100$   $\text{cm}^{-1}$ . These represent the symmetric bend ( $\nu_4$ ) and asymmetric stretch ( $\nu_3$ ) of the O–S–O (or resonant O=S=O) bonds,<sup>50</sup> respectively. A smaller peak around

$992$   $\text{cm}^{-1}$  can be attributed to the  $\nu_1$  asymmetric bend vibration mode.<sup>50</sup> Additionally, the hemihydrate phase has two peaks due to structural water at  $1637$  and  $3523$   $\text{cm}^{-1}$ . Figure 4(b) shows the evolution of the two principal sulfate peaks between  $500$  and  $1300$   $\text{cm}^{-1}$  during the different stages of the nucleation pathway from solution to the intermediate phase and to early nucleated nanometer-sized celestine ( $\sim 100$  nm range) and celestine particles that have had time to grow into considerably larger crystals ( $\geq 1$   $\mu\text{m}$ ). Infrared spectra were recorded both in solution (wet) and after filtering and drying of the solid phases. This did not significantly influence the position of the main peak locations. However, a red shift in the  $\nu_4$  vibration peak



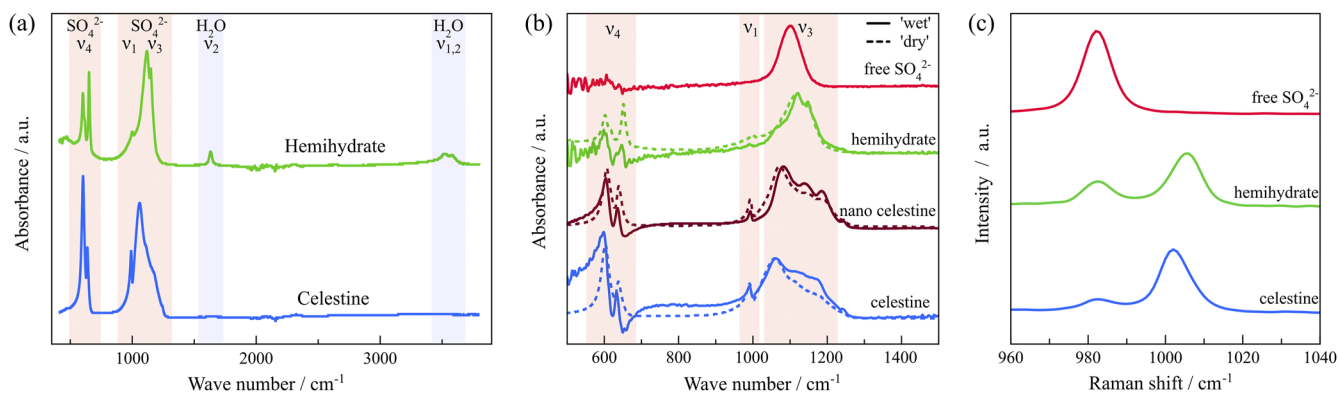


**FIG. 4.** FTIR-ATR and Raman spectra of strontium sulfate solutions, hemihydrate, and celestine. (a) FTIR spectrum of  $\text{SO}_4^{2-}$  in celestine and the hemihydrate, including the  $\nu_3$  (asymmetric stretch, around  $1100\text{ cm}^{-1}$ ) and  $\nu_4$  (asymmetric bend,  $\sim 600\text{ cm}^{-1}$ ) vibrational modes. Note the vibrational water peaks: the  $\nu_2$  (bend) peak at  $1632\text{ cm}^{-1}$  and the  $\nu_1$  and  $\nu_3$  stretching peaks between  $3500$  and  $3600\text{ cm}^{-1}$  in the hemihydrate. (b) A detailed view of  $\nu_3$  and  $\nu_4$  vibrations of  $\text{SO}_4^{2-}$  in solution and for “wet” (solid line) and “dry” (dotted line) solid phases. There is a distinct difference in  $\nu_3$  peak location for hemihydrate and celestine in both cases, as well as a significant increase in the secondary peak at  $992\text{ cm}^{-1}$  going from hemihydrate to nano-celestine to celestine. Additionally, there is a red shift in the peak for celestine as the particles grow from nanosized (light blue solid line) to bulk crystals (dark blue solid line). (c) *In situ* Raman spectra of the S=O stretch peak of free sulfate ions in solution, hemihydrate, and celestine, which was used as a probe for the transformation process.

can be observed, from  $1084$  to  $1072\text{ cm}^{-1}$ , for celestine as it grows from nanometer-sized [brown, Fig. 4(b)] particles to large bulk crystals [blue, Fig. 4(b)].<sup>51</sup> The  $\nu_1$  vibration peak at  $992\text{ cm}^{-1}$  appears to be largely absent in the hemihydrate, and increases in importance going from nano-celestine to celestine. In addition, the water peaks in the hemihydrate are also not visible in solution, and the  $\nu_4$  vibration peaks are of limited use due to the bulk water masking their signal and causing a low signal-to-noise ratio, even after subtracting the water background (Fig. S2). Consequently, we selected the  $\nu_3$  vibration to track the *in situ* evolution of the  $\text{SrSO}_4\text{-H}_2\text{O}$  system.

Raman spectra were also collected *in situ* during  $\text{SrSO}_4$  precipitation (Fig. S3). These experiments focused on the  $\nu_1$  vibration (S=O symmetric stretch), as it gives the strongest Raman signal of the sulfate vibrations [Fig. 4(c)]. We observed an absorbance maximum at  $1002\text{ cm}^{-1}$  for celestine and  $1006\text{ cm}^{-1}$  for hemihydrate, while dissolved  $\text{SO}_4^{2-}$  in solution has a maximum at  $982\text{ cm}^{-1}$ . This difference in maximum absorption energy was used to track the evolution of hemihydrate in the system.

The analytical spectroscopic and electron microscopy tools described above allow for the temporal evolution of the solid phases forming in the  $\text{SrSO}_4\text{-H}_2\text{O}$  system to be followed, but each technique comes with its own set of limitations. Specifically, electron microscopy (SEM and TEM) reveals the morphology, composition, and structure of the two crystalline phases but has not yet provided information on how these characteristics change with time. We are, however, currently undertaking studies that are based on *in situ* environmental TEM (eTEM) to provide real-time data on the transformation mechanism at sub-nanometer resolution. PXRD provides a substantial amount of structural information, but at the cost of extremely limited time resolution. Raman allows tracking of free sulfate, hemihydrate, and celestine, but the small difference between absorption peaks in the hemihydrate and celestine phases would require complex peak deconvolution algorithms and very well-refined data, thus limiting its application in mixed systems. In

comparison, FTIR can better differentiate the phases but loses the ability to track sulfate ions. Consequently, no single technique can reveal the full precipitation pathway. For this reason, the second part of this study details the use of a combination of the aforementioned methods to elucidate the transient nucleation process occurring in the strontium sulfate system.

### C. Transformation mechanism of the precursor phase to the final phase

When precipitation occurs at high supersaturations from an aqueous  $\text{SrSO}_4$  solution in a well-mixed, large-volume ( $>1\text{ ml}$ ) recipient, the hemihydrate will start to transform into celestine almost within  $\sim 5\text{ s}$  of observed nucleation. *In situ* FTIR of hemihydrate in the presence of an excess of deionized water was conducted to follow this transformation [Fig. 5(a), the graphic at the top shows the spectra collected at the start and the end of the reaction]. In this type of experiment, the entire hemihydrate signal disappears within the first 2.5 min, which is accompanied by a corresponding increase in the celestine signal. Subsequently, over a period of  $\sim 30\text{ min}$ , a red shift of one of the prominent celestine peaks occurs. As shown in Fig. 4(b), this decrease in vibrational energy occurs when celestine particles grow in size, indicating that a growth mechanism dominates after the first few minutes of celestine nucleation.

The hemihydrate Raman spectrum shown at the top of Fig. 5(b) (red curve) corresponds to the maximum concentration of hemihydrate measured at any point during the experiment. The corresponding free sulfate peak is substantially larger than the free sulfate peak for celestine after five hours (blue curve), indicating a higher solubility for hemihydrate than celestine. Based on the area under the peak corresponding to free sulfate, we find that the lowest sulfate concentration reached in the presence of hemihydrate is  $\sim 10.3 \pm 0.6\text{ mM}$ —this concentration represents an upper bound on the hemihydrate solubility in a  $100\text{ mM}$  NaCl background solution

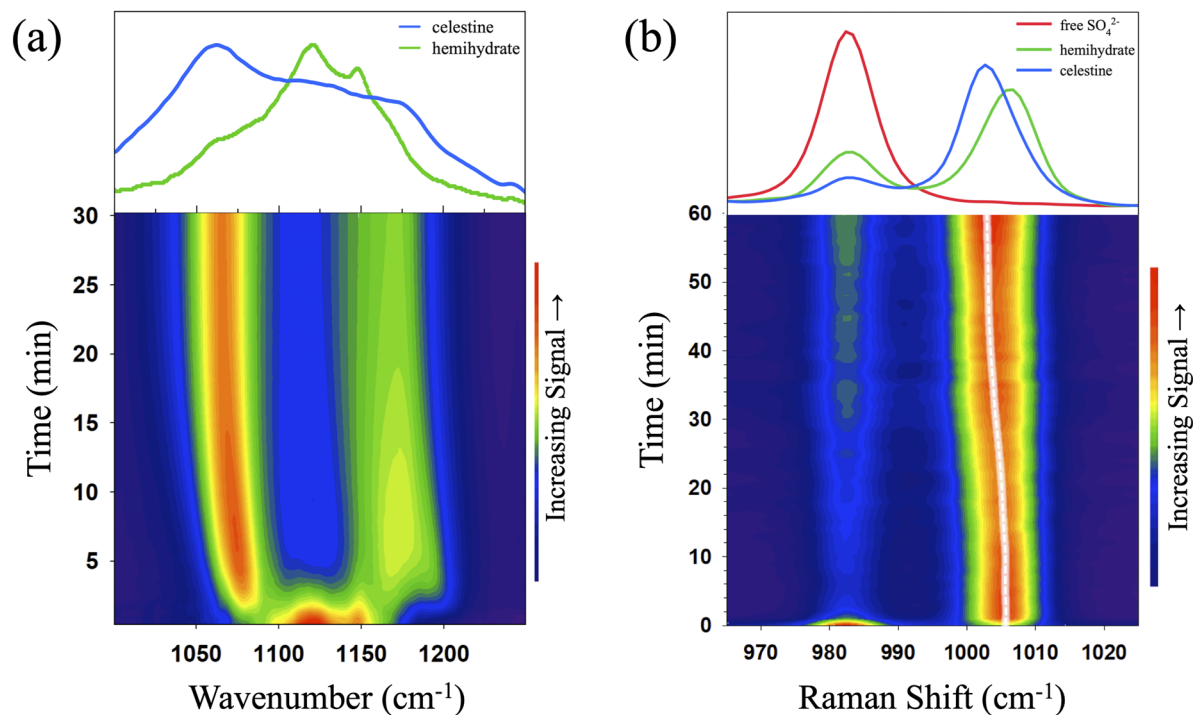


**FIG. 5.** *In situ* monitoring of the hemihydrate to celestine transformation. (a) *In situ* FTIR shows that the entire signal from the hemihydrate disappears after 5 min in the presence of excess water, and after 30 min a red shift in the strongest peak for celestine is noticeable, corresponding to the effect of particle growth on the IR signal. The top graphic displays spectra collected at the start and end of the reaction. (b) The top of the figure shows the characteristic Raman absorbance of the S=O symmetric stretch ( $\nu_1$ ) in the SrSO<sub>4</sub>-H<sub>2</sub>O system as taken from an *in situ* experiment. Free ions in solution have a peak at 982 cm<sup>-1</sup>, hemihydrate at 1006 cm<sup>-1</sup> and celestine at 1002 cm<sup>-1</sup>. All curves were normalized to the total peak area, including both solid and free ion peaks. The lower part of the figures reveals the temporal evolution of the system, including the formation and decomposition of the hemihydrate phase. The S=O stretch of the hemihydrate appears first at 1006 cm<sup>-1</sup> (green curve top graphic). As the transformation (dashed white dotted line) to celestine progresses, the peak shifts toward 1002 cm<sup>-1</sup>, which is accompanied by an increase in the free sulfate signal at 982 cm<sup>-1</sup>. This is an indication that the transformation is accompanied by the dissolution of the hemihydrate. The curve for celestine (blue curve, top graphic) was taken several hours after the experiment to allow for crystal growth.

and a lower bound on the concentration of SrSO<sub>4</sub> at which hemihydrate can precipitate. This corresponds well with the ~9–10 mM limit estimated from the induction time measurements [Fig. 1(a)]. In addition, the progress of the transformation is further characterized by a peak shift from 1004 cm<sup>-1</sup> (hemihydrate) to 1002 cm<sup>-1</sup> (celestine) during *in situ* Raman measurements [Fig. 5(b)].

Measurement of free Sr<sup>2+</sup> ions, using an ISE probe, during direct mixing reactions (i.e., adding SrCl<sub>2</sub> to Na<sub>2</sub>SO<sub>4</sub> or vice versa), revealed that after the initial consumption of Sr<sup>2+</sup> (due to the formation of the intermediate phase), a significant increase in the concentration of Sr<sup>2+</sup> indicates the onset of the phase transformation process [Fig. 6, blue curve]. In conjunction with the ISE probe, an optical probe monitored the presence of suspended particles as a function of the solution transmittance (Fig. 6, red curve). When adding SrCl<sub>2</sub> to Na<sub>2</sub>SO<sub>4</sub> within one minute of mixing, the transmittance signal drops to zero due to the formation of a gel-like phase. The early stage (<20 min) is marked by an increase in the Sr<sup>2+</sup> signal (when Na<sub>2</sub>SO<sub>4</sub> is added to SrCl<sub>2</sub>, the Sr<sup>2+</sup> signal initially decreases, inset Fig. 6), followed by the attainment of a plateau that remains stable for ~30 min. This behavior is interpreted to correspond to the removal of Sr due to the formation of the hemihydrate phase. After ~15 min, strontium ions are released back into solution (shown by

the increased signal of the ISE probe, blue curve), indicating dissolution of the metastable hemihydrate. Almost simultaneously, the transmittance signal sharply increases, corresponding to the removal of the hemihydrate gel. Finally, the free Sr<sup>2+</sup> ion concentration starts to decrease again due to the bulk formation of celestine, which concomitantly results in a rapid decrease in transmittance (red curve in Fig. 6). The lower plateau in the Sr<sup>2+</sup> signal at the end of the experiment points again to a lower solubility of celestine with respect to the hemihydrate. *In situ* Raman corroborates these findings, as it shows a similar increase in free SO<sub>4</sub><sup>2-</sup> ions during the initial stages of the transformation reaction and a final decrease in free SO<sub>4</sub><sup>2-</sup> ions at the end of the reaction [Fig. 4(b)].

*In situ* optical microscopy monitoring of an equimolar counterdiffusion experiment of SrCl<sub>2</sub> and Na<sub>2</sub>SO<sub>4</sub> solutions in a glass capillary (Fig. 7) further corroborates the idea of a dissolution-reprecipitation reaction as the main mechanism driving the transformation of the intermediate hemihydrate phase to the final celestine phase. A precipitation front formed rapidly (<30 s) at the interface between the diffusing solutions. Needle-like crystals, similar to those imaged by electron microscopy (Fig. 3), are the first macroscopic solid phases to be observed after the onset of nucleation during counterdiffusion. After several minutes, the first formed

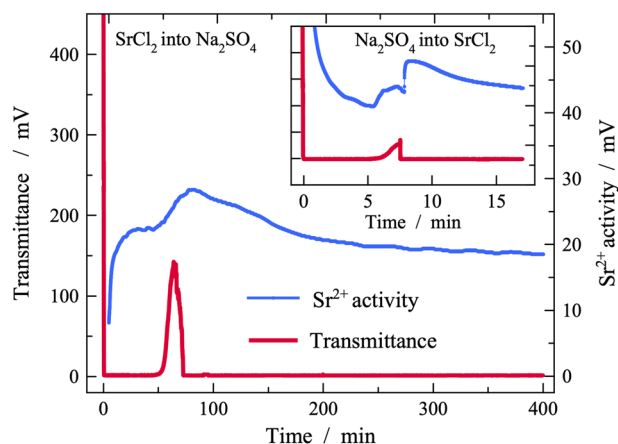


**FIG. 6.** The formation of  $\text{SrSO}_4 \cdot 1/2\text{H}_2\text{O}$  and its subsequent transformation into celestine as monitored by a transmittance probe (red curve) and an ion selective electrode (blue curve). When a stock solution of  $\text{SrCl}_2$  is titrated rapidly into a gently stirred (200 rpm) stock solution of  $\text{Na}_2\text{SO}_4$ , the capacity of the optical probe to observe changes in the solution is exceeded after the first 30 s of the precipitation reaction. The ISE indicates a plateau in the free ion concentration after the first ~25 min of reaction (indicating hemihydrate stabilization), followed by a subsequent increase in the  $\text{Sr}^{2+}$  concentration (showing dissolution of this phase). The rapid increase/decrease in the transmittance signal, coincident with the increase in ISE signal, indicates that the dissolution of the hemihydrate and nearly concomitant reprecipitation of celestine. The inset shows the results of a similar experiment conducted at a higher stirring rate (500 rpm); moreover, in this case,  $\text{Na}_2\text{SO}_4$  was added to a  $\text{SrCl}_2$  solution. The ISE signal drops until reaching a plateau (~5 min), corresponding to hemihydrate stabilization. The increased hydrodynamics speeds up the transformation process, with the increase in the ISE signal and transmittance occurring after ~7.5 min. Due to the very dense solution in these experiments, the ISE signal displays a significant amount of noise, but the overall trends are reproducible.

needles of presumably hemihydrate commence to dissolve and concomitantly particles with a morphology resembling that of celestine start to appear randomly in the central section of the capillary (i.e., at the scale of this experiment, it appears that nucleation of celestine particles is not spatially coupled to hemihydrate needles). These macroscopic results thus also support the idea that the  $\text{Sr}^{2+}$  ions released by the dissolution of the hemihydrate phase participate in the precipitation of the final phase, celestine. This corroborates the Raman and potentiometric data obtained during direct mixing experiments. It is noteworthy that the dissolution of the hemihydrate phase is first observed within the solution environment rich in  $\text{Sr}^{2+}$  and  $\text{Cl}^-$  ions—it is possible that this spatial heterogeneity is due to a stabilizing effect of  $\text{Na}^+$  or  $\text{SO}_4^{2-}$  ions on the hemihydrate.<sup>52</sup> It is also important to note that under these diffusive conditions, the full transformation of hemihydrate to celestine took ~5 h. This is in stark contrast to the much shorter transformation times noted in the other experiments (see Table I).

The above-described experiments highlight the importance of the local physicochemical environment, which appears to control the kinetics of the transformation of hemihydrate to celestine. The counterdiffusion experiment indicates that the nature of the ions surrounding the hemihydrate affects the dissolution rate of the metastable phase (i.e., faster transformation on the  $\text{SrCl}_2$  side). Moreover, in experiments in an ion-free environment (i.e.,

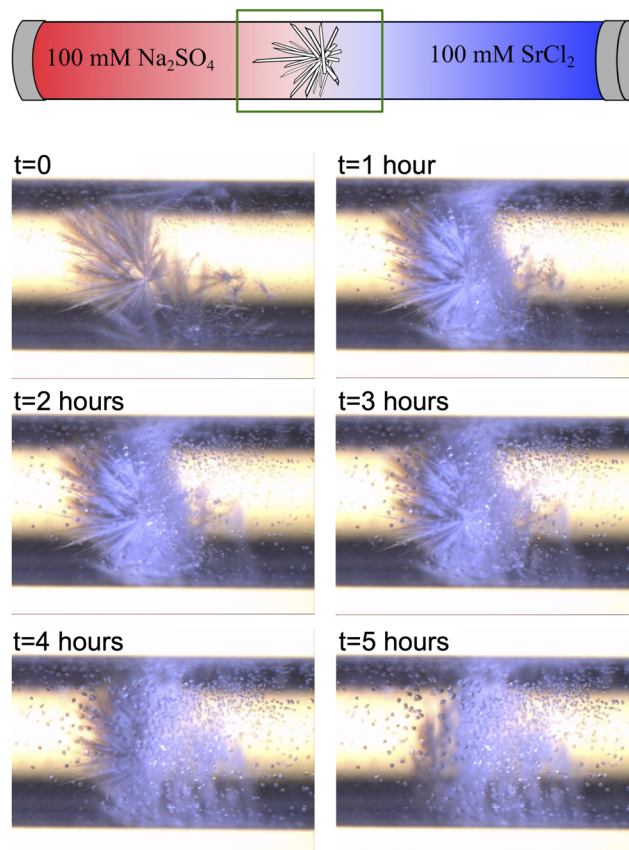


**FIG. 7.** Counter diffusion-induced  $\text{SrSO}_4$  precipitation. The uppermost schematic shows the experimental setup, including the micrograph field of view indicated by the green square. In the panels below, optical micrographs show the temporal evolution of the hemihydrate–celestine transition in a glass capillary. The first observation was achieved ~2 min after solution injection due to experimental setup time. Initially, the hemihydrate fibers appear to grow radially from nucleation points, after which the fibers exposed to  $\text{SrCl}_2$  (right side of the capillary) dissolve within the first hour. As the experiment proceeds, the fibers start to preferentially dissolve within the capillary region enriched in  $\text{SrCl}_2$  solution. The fibers progressively dissolve via a reaction front that progresses from right to left, and concomitantly, the celestine crystals located on the surface of the glass grow in size.

hemihydrate in excess deionized water, FTIR), the transformation occurs more rapidly than in a solution with a moderate ionic strength (100 mM NaCl). These observations are consistent with a previous study, which reported that the growth and dissolution rates of  $\text{BaSO}_4$  and  $\text{SrSO}_4$  can be highly dependent on the ionic strength and composition of the background electrolyte solution, an effect beyond that expected from the change in the activity coefficient of the constituent ions.<sup>53</sup> Finally, when comparing two of the direct mixing experiments (*in situ* Raman and potentiometric ISE measurements), there appears to be a difference in the kinetics, despite the fact that the only difference in reaction conditions being the method of agitation. In the Raman experiment, a double propeller mixer was used, while for the ISE experiment, a magnetic stir bar at the bottom of a beaker served to agitate the solution. This indicates that hydrodynamic considerations, and specifically the fluid

**TABLE I.** Summary of transformation times from various experiments showing that the kinetics of the reaction depends heavily on physicochemical and hydrodynamic conditions present during the experiment.

Experiment	Transformation time	Unique conditions
FTIR	3 min	No background ions
Raman	60 min	Double blade mixing (50 rpm)
Direct mixing	100 min	Stir bar mixing (500 rpm)
Diffusive mixing benchtop	5 h	Diffusion conditions
	<1 week	No bulk solution

dynamic shear rate, are another physicochemical factor influencing the reaction rate.

A remaining question regarding the dissolution-reprecipitation transformation mechanism stems from the observation that the hemihydrate phase also transformed under “dry” (i.e., when separated from the bulk liquid phase) benchtop conditions. Samples that were initially >95% pure hemihydrate were found to have transformed to celestine after as little as a week (and a maximum of two weeks) when stored in closed 50 ml plastic tubes at ambient conditions. The ambient relative humidity was estimated to have varied between 40% and 60% ( $\sim 10.9 \pm 2.2 \text{ g H}_2\text{O/m}^3$ ), based on bench top hygrometric measurements. In order to quantify the hemihydrate stability, time-resolved, semi-quantitative *in situ* PXRD (Fig. 8) in controlled relative humidity environments (70%, 80%, and 90%) was used to track the kinetics of the transformation. The results show that the rate of the hemihydrate-to-celestine reaction increases as a function of the RH. It was determined that at 90% RH, the hemihydrate has fully transformed to celestine in  $\sim 1$ d, while at 70%, approximately half of the hemihydrate has been transformed in 2.5 days. Hence, the RH-transformation experiments further support the notion that the transformation reaction is

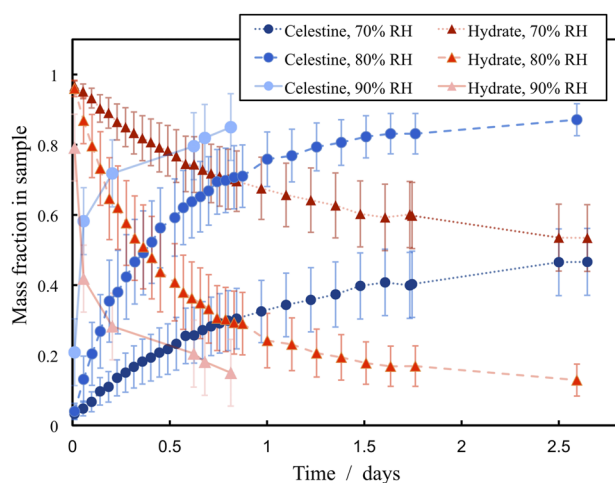


**FIG. 8.** Transformation kinetics as measured by PXRD under controlled relative humidities at 24 °C ( $100\% \text{ RH} = 21.8 \text{ g H}_2\text{O/m}^3$ ). Note that transformation rates increase with increasing humidity. Phase purity estimated by the RIR method using a Rietveld refinement of the system taken at the end of each experiment and considered a reference state.

solution-mediated and, in this particular case, driven by dissolution within a surface-adsorbed water film. The presence of adsorbed water on “dry” hemihydrate samples was confirmed by TGA measurements (Fig. S4).

#### IV. CONCLUDING REMARKS

We used a suite of experimental and analytical techniques, including Raman, FTIR, and PXRD, SEM and TEM electron microscopies, and potentiometric probes, to measure the transition from dissolved ions to the final solid phase in the  $\text{SrSO}_4\text{-H}_2\text{O}$  system at ambient conditions. Our observations revealed that in solutions with a saturation index below  $\sim 1.5$ , the early stages of nucleation are driven by bound species, akin to the prenucleation cluster model, resulting in the direct formation of celestine ( $\text{SrSO}_4$ ). At higher supersaturations, the onset of nucleation is dominated by the consumption of free ions instead of bound species. This change in nucleation mechanism is also coupled to the formation of an intermediate phase, hemihydrate ( $\text{SrSO}_4 \cdot 1/2\text{H}_2\text{O}$ ), which eventually transforms into celestine, adhering to Ostwald’s rule of stages. Importantly, the presence of a fluid appears to be crucial for this transformation process, even when present only as a fluid film due to ambient water vapor. This fluid-assisted transformation proceeds most likely via the dissolution of the metastable phase and the *de novo* crystallization of the final phase.

Multiple pathways likely exist for the dissolution-reprecipitation-mediated transformation process. Increased free-ion concentrations found during *in situ* Raman and potentiometry experiments suggest a process where the precursor hemihydrate is dissolved into a solution, creating a solution supersaturated with respect to celestine, allowing for a completely independent second nucleation event to occur. Hence, this mechanism can be viewed in terms of a classical thermodynamic-controlled process driven by chemical supersaturation in a bulk fluid. However, the phase transformation of solid hemihydrate under atmospheric conditions (benchtop and XRD) suggests a solid–fluid interfacial process may have been operative, such as coupled interfacial dissolution–reprecipitation (CIDR), as has been postulated to occur at a variety of physico-chemical conditions for minerals and glasses.<sup>58–60</sup> We also observed that the kinetics of these dissolution–reprecipitation processes strongly depend on the local physicochemical and hydrodynamic environment—in particular, the ions present, the ionic strength, and the shear rate of agitated solutions. All of these factors will influence the microchemical environment(s) associated with each fiber of the metastable phase, in particular the nature of the very thin fluid film that is known to be present at fluid–solid interfaces. This has the potential to result in very different hemihydrate behaviors in real-world environments, such as those of porous media.

Finally, the intermediate hemihydrate phase observed during the precipitation of celestine is similar in structure and metastable nature to bassanite ( $\text{CaSO}_4 \cdot 1/2\text{H}_2\text{O}$ ), a possible precursor of gypsum ( $\text{CaSO}_4 \cdot 2\text{H}_2\text{O}$ )—despite the calcium sulfate system being different in that the final phase gains water rather than losing it. However, not all alkaline earth metal sulfate systems exhibit a known hydrated intermediate phase; for example, only an anhydrous crystalline structure has been reported for  $\text{BaSO}_4$ . Thus, the nature and properties of the sulfate cation (e.g.,  $\text{Ca}^{2+}$ ,  $\text{Sr}^{2+}$ ,  $\text{Ba}^{2+}$ , etc.)

drive the stability/persistence of a (hydrated) intermediate phase and significantly influence the nucleation pathway. This underlines that although Ostwald's rule of stages is a common process, it is not a prerequisite for solid mineral formation—even in systems where it can occur. Therefore, the continuous development of our understanding of the role of the cation and its interplay with other physicochemical parameters could provide further insight on key aspects controlling the formation pathway of minerals. Overall, our results shed renewed light on the Ostwald rule of stages, and the data in these experiments suggests that the question of whether a metastable intermediate phase is formed is controlled in the prenucleation stage. Moreover, the transformation of the metastable into the final phase can follow different pathways depending on the local physico-chemical environment.

### SUPPLEMENTARY MATERIAL

See the [supplementary material](#) for details about the determination of the interfacial energy, the hemihydrate structure, infrared measurements, vibration modes for *in situ* Raman measurements, and thermogravimetric analysis.

### ACKNOWLEDGMENTS

The authors are grateful to the French national research agency, ANR, Project No. CATCH, ANR-18-CE05-0035-03. Finally, we express our gratitude to Francine Roussel at the Grenoble INP. The use of the geochemistry-mineralogy platform of ISTerre is acknowledged. The FTIR instrument was supported by funding from CPER “Montagne 4.0” and the regional platform “CEMBRO” (Changement Environnement et Biodiversité: Rétro-Observation et Observation). This work used also the platforms of the Grenoble Instruct-ERIC center (ISBG; UAR 3518 CNRS-CEA-UGA-EMBL) within the Grenoble Partnership for Structural Biology (PSB), supported by FRISBI (ANR-10-INBS-0005-02) and GRAL, financed within the University Grenoble Alpes graduate school (Ecoles Universitaires de Recherche) CBH-EUR-GS (ANR-17-EURE-0003). The electron microscope facility is supported by the Auvergne-Rhône-Alpes Region, the Fondation Recherche Medicale (FRM), the fonds FEDER, and the GIS-Infrastructures en Biologie Santé et Agronomie (IBiSA). IBS acknowledges integration into the Interdisciplinary Research Institute of Grenoble (IRIG, CEA). Finally, METSA, the French national electron microscopy and atom probe network, is also acknowledged for its initial support for eTEM work at CLYM-Lyon.

### AUTHOR DECLARATIONS

#### Conflict of Interest

The authors have no conflicts to disclose.

#### Author Contributions

**A. R. Lauer:** Data curation (equal); Formal analysis (equal); Investigation (equal); Methodology (equal); Writing – original draft (equal); Writing – review & editing (equal). **R. Hellmann:** Funding acquisition (equal); Supervision (equal); Writing – review & editing (equal). **G. Montes-Hernandez:** Methodology (supporting); Writing – review & editing (supporting). **N. Findling:** Formal analysis

(supporting); Methodology (supporting). **W. L. Ling:** Formal analysis (supporting); Methodology (supporting). **T. Epicier:** Formal analysis (equal); Methodology (equal); Writing – review & editing (equal). **A. Fernandez-Martinez:** Conceptualization (equal); Funding acquisition (equal); Methodology (equal); Supervision (equal); Writing – review & editing (equal). **A. E. S. VanDriessche:** Conceptualization (lead); Funding acquisition (equal); Methodology (equal); Supervision (equal); Writing – review & editing (lead).

### DATA AVAILABILITY

The data that support the findings of this study are available within the article and its [supplementary material](#).

### REFERENCES

- <sup>1</sup>A. E. S. Van Driessche, M. Kellermeier, L. G. Benning, and D. Gebauer, *New Perspectives on Mineral Nucleation and Growth: From Solution Precursors to Solid Materials* (Springer International Publishing, Cham, 2017).
- <sup>2</sup>E. Beniash, J. Aizenberg, L. Addadi, and S. Weiner, “Amorphous calcium carbonate transforms into calcite during sea urchin larval spicule growth,” *Proc. R. Soc. London, Ser. B* **264**(1380), 461–465 (1997).
- <sup>3</sup>L. Addadi, S. Raz, and S. Weiner, “Taking advantage of disorder: Amorphous calcium carbonate and its roles in biomineralization,” *Adv. Mater.* **15**, 959–970 (2003).
- <sup>4</sup>W. Sun and G. Ceder, “Induction time of a polymorphic transformation,” *CrystEngComm* **19**(31), 4576–4585 (2017).
- <sup>5</sup>A. E. S. Van Driessche, L. G. Benning, J. D. Rodriguez-Blanco, M. Ossorio, P. Bots, and J. M. García-Ruiz, “The role and implications of bassanite as a stable precursor phase to gypsum precipitation,” *Science* **336**(6077), 69–72 (2012).
- <sup>6</sup>S. Weiner, I. Sagi, and L. Addadi, “Structural biology. Choosing the crystallization path less traveled,” *Science* **309**(5737), 1027–1028 (2005).
- <sup>7</sup>D. Gebauer, A. Völkel, and H. Cölfen, “Stable prenucleation calcium carbonate clusters,” *Science* **322**, 1819–1822 (2008).
- <sup>8</sup>T. M. Stawski, A. E. S. Van Driessche, M. Ossorio, J. Diego Rodriguez-Blanco, R. Besslink, and L. G. Benning, “Formation of calcium sulfate through the aggregation of sub-3 nanometre primary species,” *Nat. Commun.* **7**(1), 11177 (2016).
- <sup>9</sup>T. M. Stawski, R. Besslink, K. Chatzipanagis, J. Hövelmann, L. G. Benning, and A. E. S. Van Driessche, “Nucleation pathway of calcium sulfate hemihydrate (bassanite) from solution: Implications for calcium sulfates on mars,” *J. Phys. Chem. C* **124**(15), 8411–8422 (2020).
- <sup>10</sup>D. C. Gary, M. W. Terban, S. J. L. Billinge, and B. M. Cossairt, “Two-step nucleation and growth of InP quantum dots via magic-sized cluster intermediates,” *Chem. Mater.* **27**(4), 1432–1441 (2015).
- <sup>11</sup>A. V. Radha, T. Z. Forbes, C. E. Killian, P. U. P. A. Gilbert, and A. Navrotsky, “Transformation and crystallization energetics of synthetic and biogenic amorphous calcium carbonate,” *Proc. Natl. Acad. Sci. U. S. A.* **107**(38), 16438–16443 (2010).
- <sup>12</sup>N. Krautwurst, L. Nicoleau, M. Dietzsch, I. Lieberwirth, C. Labbez, A. Fernandez-Martinez, A. E. S. Van Driessche, B. Barton, S. Leukel, and W. Tremel, “Two-step nucleation process of calcium silicate hydrate, the nanobrick of cement,” *Chem. Mater.* **30**(9), 2895–2904 (2018).
- <sup>13</sup>W. Ostwald, “Studien über die Bildung und Umwandlung fester Körper: 1. Abhandlung: Übersättigung und Überkaltung,” *Int. J. Chem. Phys.* **22U**(1), 289–330 (2017).
- <sup>14</sup>A. G. Christy, “Sulfate minerals,” in *Encyclopedia of Earth Sciences Series* (Springer, Netherlands, 2018), pp. 1392–1394.
- <sup>15</sup>A. E. S. Van Driessche, T. M. Stawski, and M. Kellermeier, “Calcium sulfate precipitation pathways in natural and engineered environments,” in *Chemical Geology* (Elsevier B.V., 2019), p. 119274.
- <sup>16</sup>T. M. Stawski, A. E. S. Van Driessche, R. Besslink, E. H. Byrne, P. Raiteri, J. D. Gale, and L. G. Benning, “The structure of CaSO<sub>4</sub> nanorods: The precursor of gypsum,” *J. Phys. Chem. C* **123**(37), 23151–23158 (2019).

- <sup>17</sup>G. Hoareau, C. Monnin, and F. Odonne, "A study of celestine equilibrium in marine sediments using the entire ODP/IODP porewater data base," *Geochim. Cosmochim. Acta* **74**(14), 3925 (2010).
- <sup>18</sup>H. M. Ezuber, "Prediction of strontium sulfate scale formation in oilfield environment," *J. ASTM Int.* **4**(6), 1–11 (2007).
- <sup>19</sup>K. D. Carrell, "The occurrence, prevention and treatment of sulphate scale in shell expro," paper presented at the SPE Offshore Europe, Aberdeen, United Kingdom, September 1987.
- <sup>20</sup>J. Ober, *Minerals Yearbook* (U.S. Geological Survey, 2020).
- <sup>21</sup>R. E. Bernstein, R. H. Byrne, P. R. Betzer, and A. M. Greco, "Morphologies and transformations of celestine in seawater: The role of acantharians in strontium and barium Geochemistry," *Geochim. Cosmochim. Acta* **56**(8), 3273 (1992).
- <sup>22</sup>A. G. Walton, "Nucleation and the interfacial tension of sparingly soluble salts," *Microchim. Acta* **51**(3), 422 (1963).
- <sup>23</sup>B. V. Enüstün and J. Turkevich, "Solubility of fine particles of strontium sulfate," *J. Am. Chem. Soc.* **82**(17), 4502 (1960).
- <sup>24</sup>D. H. Klein and J. A. Driy, "Heterogeneous and homogeneous nucleation of strontium sulphate," *Talanta* **13**(2), 289 (1966).
- <sup>25</sup>J. R. Campbell and G. H. Nancollas, "The crystallization and dissolution of strontium sulfate in aqueous solution," *J. Phys. Chem.* **73**(6), 1735 (1969).
- <sup>26</sup>J. N. Bracco, Y. Gooijer, and S. R. Higgins, "Growth kinetics of step edges on celestine (001) surfaces as a function of temperature, saturation state, ionic strength, and aqueous strontium: Sulfate ratio: An in-situ atomic force microscopy study," *Geochim. Cosmochim. Acta* **175**, 222 (2016).
- <sup>27</sup>S. He, J. E. Oddo, and M. B. Tomson, "The nucleation kinetics of strontium sulfate in NaCl solutions up to 6 m and 90 °C with or without inhibitors," *J. Colloid Interface Sci.* **174**(2), 327 (1995).
- <sup>28</sup>I. X. Malollari, P. G. Klepetsanis, and P. G. Koutsoukos, "Precipitation of strontium sulfate in aqueous solutions at 25 °C," *J. Cryst. Growth* **155**(3–4), 240 (1995).
- <sup>29</sup>A. E. Nielsen, "Nucleation and growth of crystals at high supersaturation," *Krist. Tech.* **4**(1), 17 (1969).
- <sup>30</sup>A. Packter, "The precipitation of sparingly soluble alkaline-earth metal and lead salts: Nucleation and growth orders during the induction period," *J. Chem. Soc. A* **1968**, 859.
- <sup>31</sup>M. Slovenc and B. Težak, "Kinetics and precipitation mechanism of sparingly soluble alkaline earth sulfates," *Colloid Polym. Sci.* **254**(10), 900 (1976).
- <sup>32</sup>M. Miura, H. Naono, and M. Hara, "The effect of the pH value on the crystallization of strontium sulfate in the presence of triphosphate," *Bull. Chem. Soc. Jpn.* **39**(2), 1104 (1966).
- <sup>33</sup>T. Mikami, T. Sakuma, and I. Hirasawa, "CSD-controlled reactive crystallization of SrSO<sub>4</sub> in the presence of polyethylenimine," *Chem. Eng. Res. Des.* **88**(9), 1200 (2010).
- <sup>34</sup>H. Naono, "The effect of triphosphate on the crystallization of strontium sulfate," *Bull. Chem. Soc. Jpn.* **40**(5), 1104 (1967).
- <sup>35</sup>S. Sarig and F. Tartakovsky, "Inhibition of strontium sulfate precipitation by soluble polymers," *Isr. J. Chem.* **12**(5), 905 (1974).
- <sup>36</sup>B. Lambert and W. Hume-Rothery, "CCCXLVII.—Studies of precipitated solids. Part I. Strontium sulphate," *J. Chem. Soc.* **129**, 2637–2648 (1926).
- <sup>37</sup>S. Takahashi, M. Seki, and K. Setoyama, "Formation of SrSO<sub>4</sub>·1/2H<sub>2</sub>O in an SrSO<sub>4</sub>–HO system and its solid solution in a CaSO<sub>4</sub>–SrSO<sub>4</sub>–H<sub>2</sub>O system," *Bull. Chem. Soc. Jpn.* **66**(8), 2219–2224 (1993).
- <sup>38</sup>C. M. Pina and Á. Tamayo, "Crystallisation of strontium sulphates from Si-bearing aqueous solutions," *Geochim. Cosmochim. Acta* **92**, 220 (2012).
- <sup>39</sup>G. Montes-Hernandez and F. Renard, "Time-resolved in situ Raman spectroscopy of the nucleation and growth of siderite, magnesite, and calcite and their precursors," *Cryst. Growth Des.* **16**(12), 7218–7230 (2016).
- <sup>40</sup>J. Leroux, D. H. Lennox, and K. Kay, "Direct quantitative x-ray analysis: By diffraction-absorption technique," *Anal. Chem.* **25**(5), 740–743 (1953).
- <sup>41</sup>X. Zhou, D. Liu, H. Bu, L. Deng, H. Liu, P. Yuan, P. Du, and H. Song, "XRD-based quantitative analysis of clay minerals using reference intensity ratios, mineral intensity factors, Rietveld, and full pattern summation methods: A critical review," *Solid Earth Sci.* **3**, 16 (2018).
- <sup>42</sup>A. R. Lauer, M. A. Durán-Olivencia, A. Fernandez-Martinez, and A. E. S. Van Driessche, "Multistep nucleation compatible with a single energy barrier: Catching the non-classical culprit," *Faraday Discuss.* **235**, 95–108 (2022).
- <sup>43</sup>W. J. E. M. Habraken, J. Tao, L. J. Brylka, H. Friedrich, L. Bertinetti, A. S. Schenk, A. Verch, V. Dmitrovic, P. H. Bomans, P. M. Frederik, J. Laven, P. Van Der Schoot, B. Aichmayer, G. De With, J. J. DeYoreo, and N. A. J. M. Sommerdijk, "Ion-association complexes unite classical and non-classical theories for the biomimetic nucleation of calcium phosphate," *Nat. Commun.* **4**, 1507 (2013).
- <sup>44</sup>N. A. Garcia, R. I. Malini, C. L. Freeman, R. Demichelis, P. Raiteri, N. A. J. M. Sommerdijk, J. H. Harding, and J. D. Gale, "Simulation of calcium phosphate prenucleation clusters in aqueous solution: Association beyond ion pairing," *Cryst. Growth Des.* **19**(11), 6422–6430 (2019).
- <sup>45</sup>J. Scheck, J. K. Berg, M. Drechsler, A. Kempter, A. Van Driessche, H. Cölfen, D. Gebauer, and M. Kellermeier, "New insights into the nucleation of magnesium hydroxide and the influence of poly(acrylic acid) during the early stages of Mg(OH)<sub>2</sub> crystallisation," *CrystEngComm* **24**, 7718 (2022).
- <sup>46</sup>A. Navrotsky, "Energetic clues to pathways to biomineralization: Precursors, clusters, and nanoparticles," *Proc. Natl. Acad. Sci. U. S. A.* **101**, 12096–12101 (2004).
- <sup>47</sup>F. C. Hawthorne and R. B. Ferguson, "Anhydrous sulphates I: Refinement of the crystal structure of celestine with and appendix on the structure of thenardite," *Can. Mineral.* **13**, 181–187 (1975).
- <sup>48</sup>M. Ossorio, A. E. S. Van Driessche, P. Pérez, and J. M. García-Ruiz, "The gypsum–anhydrite paradox revisited," *Chem. Geol.* **386**, 16–21 (2014).
- <sup>49</sup>U. Tritschler, A. E. S. Van Driessche, A. Kempter, M. Kellermeier, and H. Cölfen, "Controlling the selective formation of calcium sulfate polymorphs at room temperature," *Angew. Chem., Int. Ed. Engl.* **54**(13), 4083–4086 (2015).
- <sup>50</sup>M. D. Lane, "Mid-infrared emission spectroscopy of sulfate and sulfate-bearing minerals," *Am. Mineral.* **92**(1), 1–18 (2007).
- <sup>51</sup>B. Udvardi, I. J. Kovács, T. Fancsik, P. Kónya, M. Batori, F. Stercel, G. Falus, and Z. Szalai, "Effects of particle size on the attenuated total reflection spectrum of minerals," *Appl. Spectrosc.* **71**(6), 1157–1168 (2017).
- <sup>52</sup>S. Reigl, A. E. S. Van Driessche, J. Mehringer, S. Koltzenburg, W. Kunz, and M. Kellermeier, "Revisiting the roles of salinity, temperature and water activity in phase selection during calcium sulfate precipitation," *CrystEngComm* **24**, 1529–1536 (2022).
- <sup>53</sup>P. Risthaus, D. Bosbach, U. Becker, and A. Putnis, "Barite scale formation and dissolution at high ionic strength studied with atomic force microscopy," *Colloids Surf., A* **191**, 201–214 (2001).
- <sup>54</sup>R. Hellmann, J.-M. Penisson, R. L. Hervig, J.-H. Thomassin, and M.-F. Abrioux, "An EFTEM/HRTEM high resolution study of the near surface of labradorite feldspar altered at acid pH: Evidence for interfacial dissolution-reprecipitation," *Phys. Chem. Miner.* **30**, 192–197 (2003).
- <sup>55</sup>A. Putnis and C. V. Putnis, "The mechanism of reequilibration of solids in the presence of a fluid phase," *J. Solid State Chem.* **180**, 1783–1786 (2007).
- <sup>56</sup>R. Hellmann, R. Wirth, D. Daval, J.-P. Barnes, J.-M. Penisson, D. Tisserand, T. Epicier, B. Florin, and R. L. Hervig, "Unifying natural and laboratory chemical weathering with interfacial dissolution-reprecipitation: A study based on the nanometer-scale chemistry of fluid-silicate interfaces," *Chem. Geol.* **294–295**, 203–216 (2012).
- <sup>57</sup>A. Zandanel, R. Hellmann, L. Truche, V. Roddatis, M. Mermoux, G. Choblet, and G. Tobie, "Geologically rapid aqueous mineral alteration at subfreezing temperatures in icy worlds," *Nat. Astron.* **6**, 554–559 (2022).
- <sup>58</sup>T. Geisler, A. Janssen, D. Scheiter *et al.*, "Aqueous corrosion of borosilicate glass under acidic conditions: A new corrosion mechanism," *J. Non-Cryst. Solids* **356**, 1458–1465 (2010).
- <sup>59</sup>R. Hellmann, S. Cotte, E. Cadel, S. Malladi, L. S. Karlsson, S. Lozano-Perez, M. Cabié, and A. Seyeux, "Nanometre-scale evidence for interfacial dissolution-reprecipitation control of silicate glass dissolution," *Nat. Mater.* **14**, 307–311 (2015).
- <sup>60</sup>R. Hellmann, "Mechanisms of glass corrosion by aqueous solutions," in *Encyclopedia of Glass Science, Technology, History, and Culture*, 1st ed., edited by P. Richet (The American Ceramic Society, John Wiley & Sons, Inc., Hoboken, NJ, 2021), Vol. I, pp. 647–662 (invited article that reviews glass dissolution mechanisms).